

## KINETIC ENTROPY AS A DIAGNOSTIC IN PARTICLE-IN-CELL SIMULATIONS OF ASTROPHYSICAL, HELIOSPHERIC, AND PLANETARY PLASMAS

HAOMING LIANG,<sup>1</sup> PAUL A. CASSAK,<sup>1</sup> SERGIO SERVIDIO,<sup>2</sup> MICHAEL A. SHAY,<sup>3</sup> JAMES F. DRAKE, MARC SWISDAK,<sup>4</sup> MATT R. ARGALL,<sup>5</sup> JOHN C. DORELLI,<sup>6</sup> EARL E. SCIME,<sup>7</sup> WILLIAM H. MATTHAEUS,<sup>3</sup> VADIM ROYTERSHEYN,<sup>8</sup> AND GIAN LUCA DELZANNO<sup>9</sup>

<sup>1</sup>*Department of Physics and Astronomy, West Virginia University, Morgantown, WV, USA; haoming.liang@mail.wvu.edu*

<sup>2</sup>*Dipartimento di Fisica, Università della Calabria, I-87036 Cosenza, Italy*

<sup>3</sup>*Department of Physics and Astronomy, University of Delaware, Newark, DE, USA*

<sup>4</sup>*Department of Physics and Institute for Research in Electronics and Applied Physics, University of Maryland, College Park, MD, USA*

<sup>5</sup>*Physics Department and Space Science Center, Morse Hall, University of New Hampshire, Durham, NH, USA*

<sup>6</sup>*NASA Goddard Space Flight Center, Greenbelt, Maryland, USA*

<sup>7</sup>*Department of Physics and Astronomy, West Virginia University, Morgantown, WV, USA*

<sup>8</sup>*Space Science Institute, Boulder, Colorado, USA*

<sup>9</sup>*T-5 Applied Mathematics and Plasma Physics Group, Los Alamos National Laboratory, Los Alamos, NM, USA*

### ABSTRACT

We describe a systematic development of kinetic entropy as a diagnostic in fully kinetic electromagnetic particle-in-cell (PIC) simulations and investigate some of its uses to interpret plasma physics processes in astrophysical, heliospheric, and planetary systems. First, we calculate the kinetic entropy in two forms – the “combinatorial” form related to the logarithm of the number of microstates per macrostate and the “continuous” form related to  $f \ln f$ , where  $f$  is the particle distribution function. We discuss the advantages and disadvantages of each and discuss subtleties about implementing them in PIC codes. Using collisionless PIC simulations that are two-dimensional in position space and three-dimensional in velocity space, we verify the implementation of the kinetic entropy diagnostics and discuss how to optimize numerical parameters to ensure accurate results. We show the total kinetic entropy is conserved to three percent in an optimized base simulation of anti-parallel magnetic reconnection. By decomposing the kinetic entropy into a sum of a position space entropy and a velocity space entropy, we show the velocity space entropy of both electrons and ions increases in time as the plasma heats during magnetic reconnection, while the position space entropy decreases as the plasma is compressed. This project uses collisionless simulations, so it cannot address physical dissipation mechanisms; nonetheless, the infrastructure developed here should be useful for studies of collisional or weakly collisional astrophysical, heliospheric, and planetary systems. Beyond reconnection, the diagnostic is expected to be applicable to plasma turbulence and collisionless shocks.

*Keywords:* magnetic reconnection, turbulence, shock waves, plasma, Sun: flares, planets and satellites: magnetic fields

## 1. INTRODUCTION

Dissipation of energy in nearly collisionless plasmas is a key component of understanding many fundamental plasma processes, such as magnetic reconnection, plasma turbulence, and collisionless shocks. In magnetic reconnection, dissipation can change magnetic topology [e.g., Hesse et al. (2011); Cassak (2016)] and may play a role in thermalizing plasma in the exhausts [e.g., Drake et al. (2006)]. In plasma turbulence, dissipation at kinetic scales is required to terminate the energy cascade [e.g., Cranmer (2002); Parashar et al. (2009)]. A number of mechanisms for this conversion in weakly collisional plasmas have been discussed, including resonant and non-resonant wave-particle interactions and dissipation in coherent structures (*i.e.*, intermittency) such as through reconnection (Howes 2018). In collisionless shocks, dissipation is necessary to convert the upstream plasma bulk flow energy into thermal energy [e.g., Krall (1997)]. These three fundamental processes underlie a staggering array of important applications in astrophysics, heliophysics, and planetary sciences, including supernova shocks (Reynolds 2008), astrophysical jets (Beall 2014), pulsar winds (Gaensler & Slane 2006), interstellar shocks (Draine & McKee 1993), shocks in galaxy cluster mergers (Ensslin et al. 1998), solar eruptions (Priest & Forbes 2002), coronal heating (Klimchuk 2006), solar wind turbulence (Gosling 2007), solar wind-magnetosphere coupling and magnetospheric storms and substorms [e.g., Kivelson & Russell (1995)], and planetary shocks (Tsurutani & Stone 2013).

The study of dissipation is at the forefront of research in these processes and settings, but it has been challenging to study it observationally, experimentally, numerically, and theoretically [e.g., Cassak (2016); Howes (2018)]. Recently, dissipation has become more accessible to study numerically through increases in computer power and observationally through the development of high cadence satellite measurements. For example, the primary objective of the Magnetospheric Multiscale (MMS) mission (Burch et al. 2016a) is dissipation accompanying reconnection (Burch et al. 2016b), and it has also been used to study magnetosheath turbulence (Servidio et al. 2017) and the bow shock (Chen et al. 2018). Studying dissipation in solar wind turbulence would have been a key goal of the Turbulence Heating Observer (THOR) mission (Vaivads et al. 2016).

From a theoretical perspective, there have been efforts to identify regions where dissipation occurs. These measures have had some success in identifying the electron diffusion region (EDR) (Shay et al. 2007) of magnetic reconnection [e.g., Zenitani et al. (2011); Swisdak (2016); Burch et al. (2016b); Ashour-Abdalla et al. (2016)] and dissipation in reconnection exhausts (Sitnov et al. 2018), and dissipation in plasma turbulence [e.g., Wan et al. (2016); Yang et al.

(2017b,a)]. However, it is not clear which, if any, uniquely identifies genuine dissipation.

The present study is based on the premise that entropy is a natural candidate to identify and quantify dissipation. Entropy in a closed system is conserved in the absence of dissipation and monotonically increases when dissipation is present [e.g., Boltzmann (1877); Bellan (2008)]. Here, we interpret “dissipation” as a process that causes a total entropy increase in a closed, isolated system.

The fluid (thermodynamic) form of the entropy per particle for an isotropic plasma is related to  $p/\rho^\gamma$ , where  $p$  is the (scalar) pressure,  $\rho$  is the mass density, and  $\gamma$  is the ratio of specific heats. This quantity has been studied in various settings for a long time. For example, stability of Earth’s magnetotail plasma sheet to the interchange instability is governed by fluid entropy (Erickson & Wolf 1980; Borovsky et al. 1998; Kaufmann & Paterson 2006; Wolf et al. 2006; Birm et al. 2009; Wolf et al. 2009; Johnson & Wing 2009; Wang et al. 2009; Sanchez et al. 2012; Liu et al. 2014). Fluid entropy was specifically investigated in the context of magnetic reconnection, finding that it is conserved very well in magnetohydrodynamic (MHD) and particle-in-cell (PIC) simulations of reconnecting flux tubes (Birm et al. 2005, 2006). Fluid entropy has been used to identify non-adiabatic heating during reconnection (Hesse et al. 2009; Ma & Otto 2014). Lyubarsky & Kirk (2001) used fluid entropy in their study of reconnection in pulsar winds. Rowan et al. (2017) subtracted adiabatic heating from measured heating in the exhaust of a reconnection event in PIC simulations to find the leftover non-adiabatic contribution. A similar approach was used to study entropy production in collisionless shocks in PIC simulations (Guo et al. 2017, 2018).

Many astrophysical, heliophysical, and planetary settings are only weakly collisional, so the fluid approximation may or may not be applicable. Instead, a kinetic approach is likely necessary in such settings, especially in regions with fine-scale spatial or temporal structures. We follow the convention by Kadanoff (2014) and refer to the version of entropy in kinetic theory as “kinetic entropy”. The theory will be reviewed in Sec. 2.1.

Kinetic entropy has been a useful diagnostic in studies using the gyrokinetic model. In this model, the second order perturbed distribution function is related to the perturbed kinetic entropy (Krommes & Hu 1994; Schekochihin et al. 2009) and the kinetic entropy production rate is related to the heating rate (Howes et al. 2006). Using gyrokinetic and related models, energy dissipation and plasma heating have been studied in simulations of magnetic reconnection [Loureiro et al. (2013); Numata & Loureiro (2015)] and plasma turbulence [e.g., Watanabe & Sugama (2004); Tatsuno et al. (2009); TenBarge & Howes (2012); Nakata et al. (2012); TenBarge & Howes (2013); Told et al. (2015);

Li et al. (2016); Klein et al. (2017)]. Kinetic entropy has also been investigated in studies of turbulence using the Vlasov-hybrid (Vlasov ions, fluid electrons) approach (Cerri et al. 2018) and in shocks (Margolin 2017).

Meanwhile, the investigation of kinetic entropy in fully kinetic plasma systems, *i.e.*, without any degrees of freedom integrated out, has been carried out in some observational and theoretical studies. Observational data was used to study kinetic entropy in Earth’s plasma sheet (Kaufmann & Pater-son 2009, 2011) and Earth’s bow shock (Parks et al. 2012). Dynamics of the magnetosphere was investigated using various entropy measures from statistics (Balasis et al. 2009). Generalizations of kinetic entropy to kappa-distributions in the solar wind have been studied (Leubner 2004). The permutation entropy was used to analyze solar wind turbulence (Olivier et al. 2018). The entropy production in a kinetic-based fluid closure (Hammett & Perkins 1990) was recently investigated (Sarazin et al. 2009). Kinetic mechanisms for the increase of entropy have been discussed for reconnection with an out-of-plane (guide) magnetic field (Hesse et al. 2017). A recent model of the turbulent cascade employs the kinetic entropy in a renormalization group approach (Eyink 2018). However, we are not aware of any studies calculating kinetic entropy from first principles in fully kinetic PIC simulations.

There are challenges to use entropy as a diagnostic in a real system. First, the entropy can vary due to inhomogeneous plasma parameters, such as density and temperature, but mere convection should not be mistaken for dissipation. Moreover, equating an entropy increase with dissipation requires a closed system, but naturally occurring systems tend not to be closed. Despite these challenges the present approach is based on the view that studying entropy in fully kinetic models (from collisionless to collisional) in closed systems is useful to understand entropy production. The insights gained can be applied to understanding dissipation in real systems. Therefore, we argue that kinetic entropy can be a useful measure in collisionless systems, and can be crucial in collisional systems to identify dissipation. This is especially the case in the modern age of observational assets like MMS that measure particle distribution functions with a cadence of a fraction of a second and with high resolution in velocity space.

In this work, we describe a systematic development of kinetic entropy as a diagnostic in fully kinetic PIC simulations and investigate some of its uses to interpret plasma physics processes in astrophysical, heliospheric, and planetary systems. We implement two forms of kinetic entropy (Boltzmann 1877; Planck 1906) in our PIC code, the “combinatorial” and “continuous” forms. We point out that macro-particles (also known as super-particles) in a PIC simulation represent a large number of actual particles in the sys-

tem being simulated, and this needs to be properly accounted for to compare to observations or experiments. We discuss details of how to implement the diagnostic, including how to choose the velocity space grid scale and the number of macro-particles per grid cell *PPG*. It has been shown [*e.g.*, Mouhot & Villani (2011); Goldstein & Lebowitz (2004)] that kinetic entropy can be decomposed into a sum of a position space entropy and a velocity space entropy. We show that this decomposition is helpful to understand the dynamics.

We validate this diagnostic on a two-dimensional in position space, three-dimensional in velocity space collisionless PIC simulation of antiparallel magnetic reconnection, though we expect it will be equally useful for simulations of plasma turbulence and collisionless shocks. We begin by validating the implementation using a system with an analytically known kinetic entropy, *i.e.*, a system with only Maxwellian distributions. This is followed by an analysis of the kinetic entropy evolution in the simulation. We summarize our further findings here: (1) The total kinetic entropy is conserved to 3% in a carefully constructed simulation. (2) For both electrons and ions, the position space entropy decreases in time during reconnection, while the velocity space entropy increases. We will argue that this is consistent with expectations based on the physics of reconnection. (3) If one uses the combinatorial kinetic entropy, one needs to include the proper number of actual particles per simulated macro-particle to get the correct answer. (4) Using an insufficient number of macro-particles gives incorrect kinetic entropy values even though the reconnection rate is accurately modeled. This suggests caution is needed for low macro-particle per grid cell simulations on matters of kinetic entropy production, including particle acceleration and plasma heating.

It is worth noting that in the present study we develop a framework and perform a preliminary study, but we do not address the physical cause of dissipation because its presence in these simulations is purely numerical. One can show analytically that kinetic entropy increases only in the presence of collisions (Bellan 2008). Since we use a collisionless PIC code for this study, the small kinetic entropy production we detect is due to numerical effects. We leave studies of mechanisms of dissipation for future work using a collisional PIC model.

This paper is organized as follows: in Sec. 2, we review the existing theory of kinetic entropy including the fact that kinetic entropy can be decomposed into position and velocity space entropies. Section 3 contains a thorough discussion of implementing the kinetic entropy diagnostic into PIC codes. Section 4 describes the setup of the simulations we employ. Section 5 shows the simulation results, including a discussion of how to choose the diagnostic and simulation parameters to achieve robust results and a discussion of using kinetic

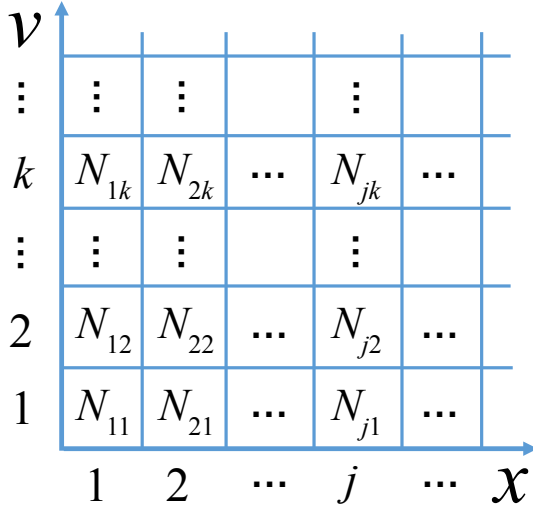


**Figure 1.** Sketch of phase space  $(x, v)$  for a 1D system, discretized into a grid. The number of particles in the bin spanning position  $x_j$  to  $x_j + \Delta x$  and velocity  $v_k$  to  $v_k + \Delta v$  is  $N_{jk}$ . This can be suitably extended to higher dimensional systems.

entropy to obtain physical insights. Finally, conclusions, applications, and future work are discussed in Sec. 6.

## 2. THEORY

### 2.1. Background on Kinetic Entropy

For a closed system (which in Nature could be thermally insulated, but in a simulation can also be periodic), the form of kinetic entropy  $\mathcal{S}$  in a kinetic framework is (Boltzmann 1877; Planck 1906)

$$S(t) = k_B \ln \Omega(t), \quad (1)$$

where  $k_B$  is Boltzmann's constant and  $\Omega(t)$  is the number of microstates of the system that produce the system's macrostate at a time  $t$ . In what follows, we suppress the time dependence to simplify the notation. Each individual plasma species has its own associated kinetic entropy, so there is an implicit subscript  $e$  or  $i$  for electrons or ions, respectively, that is suppressed for clarity when possible. Following the nomenclature in Frigg & Werndl (2011), we refer to the kinetic entropy in this form as the ‘‘combinatorial Boltzmann entropy.’’ This is one form of kinetic entropy we implement in our PIC code.

To elucidate the meaning of kinetic entropy in this form, consider a plasma with a fixed number of charged particles  $N$  for each species. We treat classical, non-relativistic systems (even though the PIC code we use is fully relativistic).

For a three-dimensional (3D) system, phase space is 6D with each particle described by its position and velocity  $(\vec{r}, \vec{v})$ . To calculate kinetic entropy, phase space is discretized into domains we call bins. Figure 1 shows the discretization of

an analogous 1D system. Define  $N_{jk}$  as the number of particles in the phase space bin spanning positions  $\vec{r}_j$  to  $\vec{r}_j + \Delta\vec{r}$  and velocities  $\vec{v}_k$  to  $\vec{v}_k + \Delta\vec{v}$  at a given time  $t$ , where the components of  $\Delta\vec{r}$  and  $\Delta\vec{v}$  describe the extent of the bin in each direction in phase space. At this point, we nominally take these bins as finite in size (*i.e.*, not infinitesimal) with an eye to calculating kinetic entropy in PIC simulations. The volumes of the bins in position and velocity space are  $\Delta^3 r$  and  $\Delta^3 v$ , respectively. In a 1D system, subscripts  $j$  and  $k$  signify the bin in position space and velocity space, respectively. In 3D, we continue to use  $j$  and  $k$  as shorthand to identify the bin, even though we actually need to specify each component of the position and velocity to identify a bin. Thus, we think of  $j$  to mean  $j_x, j_y, j_z$  for the  $x, y, z$  directions in position space and  $k$  to mean  $k_x, k_y, k_z$  for the  $v_x, v_y, v_z$  directions in velocity space. By definition,

$$N = \sum_{j,k} N_{jk}. \quad (2)$$

A given macrostate is defined by the collection of all the  $N_{jk}$ , which via integration yields all the fluid quantities of the system. A microstate is a possible way to choose the particles in the system to produce a given macrostate, treating individual particles classically as distinguishable.

Using this construct, the number  $\Omega$  of possible microstates for a given macrostate is calculated using combinatorics [see, *e.g.*, Bellan (2008)]; it is the number of permutations that produce the macrostate with  $N_{jk}$  particles in the  $jk$ th cell by swapping individual distinguishable particles between any of the bins, *i.e.*,

$$\Omega = \frac{N!}{\prod_{j,k} N_{jk}!}. \quad (3)$$

Inserting this expression into Eq. (1) and simplifying gives the combinatorial Boltzmann entropy  $\mathcal{S}$  in terms of the  $N_{jk}$ :

$$\mathcal{S} = k_B \left[ \ln N! - \sum_{j,k} \ln N_{jk}! \right]. \quad (4)$$

The first term is a constant assuming the total number of particles  $N$  in the closed system is fixed. Since only changes in entropy are physically important, we can drop the first term if desired (though we retain it in the calculation of the combinatorial Boltzmann entropy in our PIC simulations). Note, however, that whether the first term is retained or not, quantities like percentage changes in entropy should be calculated solely relative to the second term.

It is common to approximate Eq. (4) using Stirling's approximation  $\ln N_{jk}! \approx N_{jk} \ln N_{jk} - N_{jk}$ , which is valid when  $N_{jk} \gg 1$ , as is typically the case but may have exceptions. A short calculation using Eq. (2) yields

$$S = k_B \left[ N \ln N - \sum_{j,k} N_{jk} \ln N_{jk} \right], \quad (5)$$

where we write the approximate entropy as  $S$  instead of  $\mathcal{S}$ . For use in a kinetic description of a fluid or plasma, one writes the kinetic entropy in terms of the distribution function  $f(\vec{r}, \vec{v})$ . The distribution function at position  $\vec{r}_j$  and velocity  $\vec{v}_k$  is approximated as

$$f(\vec{r}_j, \vec{v}_k) \approx \frac{N_{jk}}{\Delta^3 r \Delta^3 v}. \quad (6)$$

Replacing  $N_{jk}$  in Eq. (5) with this expression and simplifying gives

$$S = k_B \left[ N \ln \left( \frac{N}{\Delta^3 r \Delta^3 v} \right) - \sum_{j,k} (\Delta^3 r \Delta^3 v) f(\vec{r}_j, \vec{v}_k) [\ln f(\vec{r}_j, \vec{v}_k)] \right]. \quad (7)$$

As in Eq. (4), the first term is a constant (for a fixed phase space bin size) and can be discarded. In the limit in which  $\Delta \vec{r}$  and  $\Delta \vec{v}$  are small, the second term yields the commonly used form of the kinetic entropy

$$S = -k_B \int d^3 r d^3 v f(\vec{r}, \vec{v}) [\ln f(\vec{r}, \vec{v})], \quad (8)$$

where  $d^3 r$  and  $d^3 v$  are the infinitesimal spatial and velocity space volumes. Following the nomenclature of Frigg & Werndl (2011), we refer to Eq. (8) as the ‘‘continuous Boltzmann entropy’’ to distinguish it from the combinatorial Boltzmann entropy  $\mathcal{S}$ . This is the second form of kinetic entropy we implement in our PIC code. Note that in dropping the first term of Eq. (7), there is an issue with the units of  $S$  in that the second term is no longer formally dimensionless. Therefore, care is necessary when the continuous Boltzmann entropy is desired in proper units. We discuss this in more detail in Sec. 3.4.

We note in passing that one can alternately normalize  $f$  to be a probability density rather than a phase space density. In this convention, the entropy would be related to the Shannon entropy and information theory (Shannon 1948; Jaynes 1963). We do not employ this convention here with an eye to experiments and observations that directly measure distribution functions.

The continuous Boltzmann entropy density, *i.e.*, the continuous Boltzmann entropy per unit volume, is denoted by  $s(\vec{r})$  and given by

$$s(\vec{r}) = -k_B \int d^3 v f(\vec{r}, \vec{v}) [\ln f(\vec{r}, \vec{v})]. \quad (9)$$

We point out that the continuous Boltzmann entropy density  $s_M(\vec{r})$  for a 3D drifting Maxwellian distribution in local thermodynamic equilibrium (LTE) for a species of mass  $m$ , number density  $n(\vec{r})$ , bulk flow velocity  $\vec{u}(\vec{r})$ , and temperature

$T(\vec{r})$ , with  $f(\vec{r}, \vec{v}) = f_M = n(\vec{r}) [m/2\pi k_B T(\vec{r})]^{3/2} e^{-m[\vec{v}-\vec{u}(\vec{r})]^2/2k_B T(\vec{r})}$ , is exactly solvable with

$$s_M(\vec{r}) = \frac{3}{2} k_B n(\vec{r}) \left[ 1 + \ln \left( \frac{2\pi k_B T(\vec{r})}{m n^{2/3}(\vec{r})} \right) \right]. \quad (10)$$

This result shows the fluid entropy per particle  $s/n$  is related to  $p/\rho^\gamma$ , where  $p = nk_B T$  is the (scalar) pressure,  $\rho = mn$  is the mass density, and  $\gamma = 5/3$  is the ratio of specific heats. In an adiabatic process, conservation of  $s/n$  is synonymous with conservation of  $p/\rho^\gamma$ , which is typically used in fluid models. We use Eq. (10) later to validate the implementation of the kinetic entropy diagnostic in our PIC code.

## 2.2. Decomposition of Kinetic Entropy into Position and Velocity Space Entropies

Boltzmann’s kinetic entropy is defined in terms of permutations of particles with any position and velocity in phase space. It is tempting to interpret the kinetic entropy density in Eq. (9) as the entropy purely associated with permuting particles in velocity space, but this is only correct if the plasma density is uniform. If the density is non-uniform (*i.e.*,  $n$  is a function of  $\vec{r}$ ), it has been shown that the total kinetic entropy can be decomposed into a sum of a position space entropy and a velocity space entropy [*e.g.*, Mouhot & Villani (2011); Goldstein & Lebowitz (2004)], as we now review.

By adding and subtracting a common term in Eq. (4),  $k_B \sum_j N_j!$ , where  $N_j = \sum_k N_{jk}$  is the total number of particles in spatial cell  $j$ , *i.e.*, with any velocity, the combinatorial Boltzmann entropy  $\mathcal{S}$  can be written as

$$\mathcal{S} = k_B \left[ \ln N! - \sum_j \ln N_j! \right] + k_B \sum_j \left[ \ln N_j! - \sum_k \ln N_{jk}! \right]. \quad (11)$$

The first two terms have the same form as Eq. (4), except that the second term has  $N_j!$  instead of  $N_{jk}!$ , so they are defined as the position space kinetic entropy,

$$\mathcal{S}_{\text{position}} = k_B \left[ \ln N! - \sum_j \ln N_j! \right]. \quad (12)$$

Similarly, the last two terms in Eq. (11) have the same form as Eq. (4) with  $N$  replaced by  $N_j$  and the summation being only over velocity space, so they are defined as the velocity space kinetic entropy

$$\mathcal{S}_{\text{velocity}} = \sum_j k_B \left[ \ln N_j! - \sum_k \ln N_{jk}! \right]. \quad (13)$$

Consequently, Eq. (11) can be written as

$$\mathcal{S} = \mathcal{S}_{\text{position}} + \mathcal{S}_{\text{velocity}}, \quad (14)$$

so the combinatorial Boltzmann entropy is decomposed into a sum of position space kinetic entropy and velocity space kinetic entropy.

Note that there is an asymmetry between the treatment of position and velocity space in this definition of the position space entropy and velocity space entropy. The number of microstates per macrostate is calculated in velocity space for each spatial cell to obtain velocity space entropy, while the position space entropy is obtained by summing over velocity space first. Alternatively, one could interchange the treatment of position and velocity space in this calculation. Therefore, the decomposition used here is not unique. However, the decomposition employed here and elsewhere gives meaningful information about local velocity space entropy changes that are indicative of heating or dissipation, which makes it a preferred decomposition.

As in Sec. 2.1, one can readily derive expressions for the position and velocity space kinetic entropies in terms of the distribution function and analogous expressions in terms of the plasma density  $n$ ; using Stirling's approximation assuming there are a large number of particles, one obtains the discrete forms of the continuous Boltzmann position and velocity space kinetic entropies as

$$S_{\text{position}} = k_B \left[ N \ln \left( \frac{N}{\Delta^3 r} \right) - \sum_j (\Delta^3 r) n(\vec{r}_j) \ln n(\vec{r}_j) \right], \quad (15)$$

$$S_{\text{position}} = \sum_j (\Delta^3 r) s_{\text{position}}(\vec{r}_j), \quad (16)$$

$$s_{\text{position}}(\vec{r}_j) = k_B \left[ n(\vec{r}_j) \ln \left( \frac{N}{\Delta^3 r} \right) - n(\vec{r}_j) \ln n(\vec{r}_j) \right], \quad (17)$$

$$S_{\text{velocity}} \equiv \sum_j (\Delta^3 r) s_{\text{velocity}}(\vec{r}_j), \quad (18)$$

$$s_{\text{velocity}}(\vec{r}_j) = k_B \left[ n(\vec{r}_j) \ln \left( \frac{n(\vec{r}_j)}{\Delta^3 v} \right) - \sum_k (\Delta^3 v) f(\vec{r}_j, \vec{v}_k) \ln f(\vec{r}_j, \vec{v}_k) \right], \quad (19)$$

where  $n(\vec{r}_j) = N_j/\Delta^3 r$  is the number density at spatial cell  $j$ . Expressions in terms of continuous variables come from

taking the limit of small bin size gives

$$S_{\text{position}} = k_B \left[ N \ln \left( \frac{N}{\Delta^3 r} \right) - \int d^3 r n(\vec{r}) \ln n(\vec{r}) \right], \quad (20)$$

$$S_{\text{position}} = \int d^3 r s_{\text{position}}(\vec{r}), \quad (21)$$

$$s_{\text{position}}(\vec{r}) = k_B \left[ n(\vec{r}) \ln \left( \frac{N}{\Delta^3 r} \right) - n(\vec{r}) \ln n(\vec{r}) \right], \quad (22)$$

$$S_{\text{velocity}} = \int d^3 r s_{\text{velocity}}(\vec{r}), \quad (23)$$

$$s_{\text{velocity}}(\vec{r}) = k_B \left[ n(\vec{r}) \ln \left( \frac{n(\vec{r})}{\Delta^3 v} \right) - \int d^3 v f(\vec{r}, \vec{v}) \ln f(\vec{r}, \vec{v}) \right]. \quad (24)$$

Note, the second term in  $s_{\text{velocity}}(\vec{r})$  is merely  $s(\vec{r})$  from Eq. (9), so the two differ by the first term. The key point is that the kinetic entropy density  $-k_B \int d^3 v f \ln f$  is not the velocity space entropy because of this extra term. Only in the limit in which  $n(\vec{r})$  is uniform are the two effectively the same. Also, by adding  $s_{\text{position}}(\vec{r})$  to the  $s_{\text{velocity}}(\vec{r})$ , one obtains Eq. (9) plus a term related to  $n(\vec{r})$ . The integral over space of the latter term is the first (constant) term in Eq. (7).

The physical meaning of the position and velocity space entropies are given by analogies with the combinatorial Boltzmann entropy  $\mathcal{S}$ . The position space entropy describes the entropy arising from permutations of particles in position space without regard to their velocity. For example, there is only one way to have all the particles in a single bin in position space;  $\Omega = 1$  for that system and the position space entropy is zero. In contrast, a uniform density has the largest number of microstates that produce that macrostate, so it is the configuration with the largest position space entropy. Therefore, compressing a plasma increases the local density, so is associated with a local decrease in position space entropy.

The velocity space entropy has a similar interpretation – it is the entropy associated with the permutation of particles in velocity space at a fixed cell in phase space, then summed over all spatial bins. As with the position space entropy, more distributed particles in velocity space are associated with higher velocity space entropy, while sharper (colder) distributions have lower velocity space entropies. Increases in density and temperature both lead to an increase in velocity space entropy, as is seen explicitly for a Maxwellian distribution in Eq. (10). Note, for an adiabatic process for a system in local thermodynamic equilibrium, the total entropy is conserved. However, the position and velocity space entropies can change, with kinetic entropy converted between

them. During adiabatic compression, for example, the position space entropy decreases as described above. This decrease is perfectly balanced by adiabatic heating which increases the velocity space entropy. We find the decomposition into position and velocity space entropies provides useful insights in the analysis of the PIC simulations that follow.

### 3. IMPLEMENTATION OF KINETIC ENTROPY DIAGNOSTIC IN PIC SIMULATIONS

In this section, we provide a detailed summary of how we implement the kinetic entropy diagnostic into our PIC code P3D (Zeiler et al. 2002), although the approach should be applicable to any explicit PIC code. We emphasize that we use periodic boundary conditions so that the system is closed and one can unambiguously determine if there are global changes in kinetic entropy (as opposed to open systems where the kinetic entropy can change via dynamics at the boundary). In what follows, we break down the procedure into steps and discuss each in turn.

#### 3.1. Macro-particles vs. Actual Particles

As discussed in Sec. 2.1, calculating the combinatorial  $\mathcal{S}$  or continuous  $S$  Boltzmann entropies requires a knowledge of the number of particles in each cell in phase space. In a PIC simulation, the “particles” are actually macro-particles, each representing a chunk of phase space containing a large number of actual particles. Therefore, there is a difference between the number of particles and number of macro-particles in each cell. As we show here, the relative structure of the continuous Boltzmann entropy  $S$  is not sensitive to this difference. However, when converting  $S$  from a PIC simulation into real units, the results are sensitive to this difference. Moreover, the combinatorial Boltzmann entropy  $\mathcal{S}$  is sensitive to the number of actual particles represented by each macro-particle.

Here, we discuss how to relate the number of macro-particles to the number of actual particles. We define a constant  $a$  as the number of actual particles per macro-particle. The approach to estimate  $a$  is to find the number of actual particles, say, electrons, that would be in a given grid cell in the simulation. For a system with a known number density  $n$ , the number of electrons  $N_{cell}$  in a spatial volume  $\Delta^3 r$  corresponding to a grid cell in PIC is

$$N_{cell} \sim n\Delta^3 r. \quad (25)$$

A typical grid size for an explicit PIC simulation is close to the electron Debye length  $\lambda_{De} = (\epsilon_0 k_B T_e / n_e e^2)^{1/2}$ . Thus,  $N_{cell}$  is on a similar scale as the plasma parameter  $n\lambda_{De}^3$ . For reference, representative values for the plasma parameter in various settings are provided in Table 1, though of course these are merely representative and may differ for particular applications.

To get a comparable number for the PIC code in order to find  $a$ , we note that many PIC codes, including the one in use here, allow for macro-particles to be assigned a different weight  $W$ , which improves the statistics in systems with non-uniform initial densities. This must be accounted for in the estimation of  $N_{cell}$ . We now estimate  $N_{cell}$  using the initial conditions of the simulations carried out for the present study. At  $t = 0$  in our simulations,  $W$  is same for all macro-particles in each grid cell and is proportional to the local density. Thus,  $PPG \times W$  represents the effective number of macro-particles per grid cell, so at  $t = 0$  the number of actual particles in a cell is

$$N_{cell} = PPG \times W \times a. \quad (26)$$

Equating the two expressions for  $N_{cell}$  from Eqs. (25) and (26) gives

$$a = \frac{n\Delta^3 r}{PPG \times W}. \quad (27)$$

In simulations for which  $W$  is not a constant for all particles in each cell, a generalization of this approach is necessary.

It is important to note when and how including  $a$  is necessary in calculating kinetic entropy. Define  $\mathcal{N}_{jk}$  as the number of weighted macro-particles in the  $jk$ th bin in phase space; then

$$N_{jk} = a\mathcal{N}_{jk}. \quad (28)$$

The value for  $\mathcal{N}_{jk}$  is what one gets from the code when counting weighted macro-particles, but does not take into account the number of actual particles per macro-particle. Physically, because the limited number of macro-particles in a PIC simulation implies that there is a small number of macro-particles per phase space bin, the number of permutations of the macro-particles is much smaller than the number of permutations of actual particles. Therefore, if one uses  $\mathcal{N}_{jk}$  instead of  $N_{jk}$  to calculate Eq. (4), the result is much smaller than that of actual system. More importantly, the Stirling approximation and thus the continuous Boltzmann entropy  $S$  definition would be invalid since  $\mathcal{N}_{jk}$  is small. The importance of including  $a$  can be seen analytically, as well. Writing Eq. (4) in terms of  $\mathcal{N}_{jk}$  gives  $\mathcal{S} = k_B[\ln(a\mathcal{N})! - \sum_{j,k} \ln(a\mathcal{N}_{jk})!]$ , which is not equal to  $ak_B[\ln\mathcal{N}! - \sum_{j,k} \ln\mathcal{N}_{jk}!]$ . Thus, the value for  $a$  must be included at calculation time to get the proper value of the combinatorial Boltzmann entropy  $\mathcal{S}$ .

In contrast, the kinetic entropy (*i.e.*, after using the Stirling approximation) is simply linear in  $a$ . Using  $N = a\mathcal{N}$  and  $N_{jk} = a\mathcal{N}_{jk}$  in Eq. (5) gives

$$S = k_B \left[ a\mathcal{N} \ln(a\mathcal{N}) - \sum_{j,k} a\mathcal{N}_{jk} \ln(a\mathcal{N}_{jk}) \right]. \quad (29)$$

Carrying out simple manipulations gives

$$S = ak_B \left[ \mathcal{N} \ln\mathcal{N} - \sum_{j,k} \mathcal{N}_{jk} \ln\mathcal{N}_{jk} \right]. \quad (30)$$

**Table 1.** Representative values of the plasma parameter  $n\lambda_{De}^3$  in a number of plasma settings (Ji & Daughton 2011; Rosenberg et al. 2015; Naval Research Laboratory Plasma Physics Division 2018).

Setting	Density (cm <sup>-3</sup> )	$T_e$ (eV)	$n\lambda_{De}^3$
Solar active region	10 <sup>9</sup>	100	$1.3 \times 10^7$
Magnetotail	0.2	500	$1.0 \times 10^{13}$
MRX reconnection experiment	$(0.1 - 1) \times 10^{14}$	5-15	450-7,000
Solar wind at 1 AU	10	10	$4.1 \times 10^9$
Magnetosheath	20	50	$3.2 \times 10^{10}$
Earth's ionosphere	10 <sup>6</sup>	0.01-0.1	410-13,000
High energy density laser plasma	10 <sup>20</sup>	1000	1,300

Thus, one can simply calculate the continuous Boltzmann entropy using macro-particles in the simulation, and then scale the result by  $a$  to get a value for  $S$ . The same result holds for the forms in terms of the distribution function  $f$  [*i.e.*, Eq. (8) and (9)]. In other words, if comparing  $f$  or  $S$  between a PIC simulation and observations or experiments and an absolute comparison is desired, one must multiply the raw  $f$  and  $S$  from the simulation by  $a$  to convert it to a physical result.

### 3.2. Binning Macro-Particles in Phase Space

In order to obtain the distribution function, one has to discretize phase space (with bins from  $\vec{r}_j, \vec{v}_k$  to  $\vec{r}_j + \Delta\vec{r}, \vec{v}_k + \Delta\vec{v}$ ) and calculate the contribution of each macro-particle to every phase space bin. There are numerous approaches to representing the number density of a macro-particle in a PIC code, referred to as its shape (Birdsall & Langdon 2004). The approach used in P3D, and therefore applied here, is a linear shaping function that assumes the charge density from each macro-particle drops linearly from its maximum to zero a distance one spatial grid cell away in each direction. Therefore, in any PIC simulation without a  $\delta$ -function shaping function, a macro-particle contributes to the density in each of the surrounding cells. To calculate kinetic entropy, we use the same shape function for each particle in velocity space (*i.e.*, linear). Therefore, the number of macro-particles in a phase space bin at any given time is typically not an integer. We suggest that the implementation of the kinetic entropy calculation should employ the same particle shape as what is employed in the code in use, but leave further investigation to future work.

Here is the procedure we use for determining the number of macro-particles in each phase space bin:

- Without using the kinetic entropy diagnostic, optimize the numerical parameters on a test simulation to en-

sure proper spatial and temporal resolution. Using the output from this simulation, find the maximum speed  $v_{max}$  among all macro-particles for all times, which should be  $\ll c$  in the non-relativistic limit. Then, the range of velocity space to be discretized is restricted to  $[-v_{max}, v_{max}]$ . We use the same velocity range for each velocity component and for all time. (One could choose  $v_{max} = c$  without doing a test simulation first, but for non-relativistic systems one would have many phase space cells with no particles, which leads to wasted memory and longer computational times for fixed velocity space bin size.)

- Discretize velocity space by defining a velocity bin size  $\Delta v$ , which we choose to be the same in each direction in velocity space. The velocity space bin size should be small enough to resolve typical velocity distribution functions, but large enough to preserve reasonably good statistics without many bins lacking particles, which leads to longer computational times. If the velocity distributions in a system have known theoretical kinetic entropy values, a good way to determine  $\Delta v$  is to compare the results using different  $\Delta v$  with the predicted values, as we discuss further in Sec. 5.6. We find that using a velocity space bin size comparable to the thermal speed is a good choice for the parameters of our simulation.

Since  $\Delta v$  determines the constant terms in Eqs. (7), (19) and (24), an absolute comparison of kinetic entropies of species with different  $\Delta v$  would not be meaningful. Instead, only relative changes to kinetic entropy should be used in such a case. Therefore, for this initial study, we choose parameters so that the ion and electron thermal speeds are comparable, so we can use the same  $\Delta v$  for both electrons and ions and be able



to make direct comparisons. For systems for which  $v_{th,e}$  and  $v_{th,i}$  are different, one should use different bin sizes for each species. It is important to note that once the velocity space bin size for each species is set, it should be held fixed for the duration of the simulation and should be the same size for all grid cells. These constraints are necessary to be able to compare kinetic entropies at different times and at different locations.

- Choose a spatial bin size  $\Delta x$ . In principle, this need not be the same as the grid scale  $\Delta x$ , but this is the most logical choice and what we employ here.
- Cycle over every macro-particle and find the number density contribution to each spatial bin using the particle shape in the code, and increment its contribution to the number of macro-particles in the appropriate phase space bin based on the three components of the macro-particle's velocity. The end result after counting all macro-particle contributions to every phase space bin is the total number of macro-particles in every bin  $N_{jk}$ . Recall, this typically is not an integer.
- If one wants to calculate the combinatorial Boltzmann entropy  $\mathcal{S}$ , then multiply  $N_{jk}$  in each bin by  $a$  to get  $N_{jk}$ . As discussed in Sec. 3.1, multiplying by  $a$  at calculation time is not necessary for the continuous Boltzmann entropy  $S$ , but it would lead to an incorrect value of the combinatorial Boltzmann entropy  $\mathcal{S}$ .

Spatial cells at the boundary of a computational domain need to get information from other processors for macro-particles in nearby cells that contribute to  $N_{jk}$ . This leads to an increase in run time; for the present study, the ‘‘base’’ simulation takes 13% more time than the same simulation without calculating the kinetic entropy. We believe this performance could be improved, but leave that for future work.

### 3.3. Calculating Distribution Functions and Kinetic Entropies

The distribution function  $f(\vec{r}_j, \vec{v}_k)$  at bin  $\vec{r}_j$  and  $\vec{v}_k$  is immediately approximated from  $N_{jk}$  using Eq. (6). Once  $f$  is obtained for all velocity space bins in all spatial cells, the forms of continuous Boltzmann entropy are readily calculated, such as Eq. (7) for  $S$ , the discretized version of Eq. (9) for  $s(\vec{r}_j) = -k_B \sum_k (\Delta^3 v) f(\vec{r}_j, \vec{v}_k) \ln[f(\vec{r}_j, \vec{v}_k)]$ , and Eq. (19) for  $S_{\text{velocity}}$ . Note  $S_{\text{position}}$  in Eq. (15) does not require the distribution function.

To find the combinatorial Boltzmann entropy  $\mathcal{S}$ , use Eq. (4). Since the  $N_{jk}$  are not integers, the factorial in Eq. (4) needs to be reinterpreted using the  $\Gamma$  function for which  $\Gamma(N+1) = N!$  for integer  $N$  [e.g., Arfken & Weber (1995)] as

$$\mathcal{S} = k_B \left[ \ln[\Gamma(N+1)] - \sum_{j,k} \ln[\Gamma(N_{jk}+1)] \right]. \quad (31)$$

Note that  $N_{jk}$  need not be large in every cell, so the non-integer part should not be ignored. Fortunately, many programming languages contain an intrinsic function for  $\ln[\Gamma(x)]$ , so the calculation is efficient and there are no issues with performing this calculation for large argument [while calculating  $\Gamma(N+1)$  separately would lead to numerical problems for large arguments]. A similar calculation can be used to get the combinatorial Boltzmann entropy for position and velocity space from Eqs. (12) and (13), respectively.

### 3.4. Merits of Combinatorial vs. Continuous Boltzmann Entropy

We close this section with a discussion of the relative merits between the combinatorial  $\mathcal{S}$  and continuous  $S$  Boltzmann kinetic entropies. Three advantages of the combinatorial Boltzmann entropy are that it is the most accurate form of kinetic entropy (it does not rely on assuming  $N_{jk} \gg 1$ ), it is automatically in appropriate units, and the intrinsic `LNGAMMA` function in many coding languages makes the calculations efficient and more importantly can be calculated for large argument, whereas a direct calculation taking the factorial of a large number is not possible. A drawback of the combinatorial Boltzmann entropy is that the value of  $a$ , describing the number of actual particles per macro-particle, must be included from the beginning in the calculation. Thus, if one wants to see how the combinatorial Boltzmann entropy changes between two different values of  $a$ , one must redo the calculation of kinetic entropy with a different  $a$  value.

The continuous Boltzmann entropy  $S$  has the advantage that one does not need to specify  $a$  at run-time. Therefore, finding the kinetic entropy for the same simulation but with a different  $a$  is trivial and does not require redoing the calculation. A disadvantage of the continuous Boltzmann entropy is that one has to make sure that  $a$  is large enough that the errors in Stirling's approximation are small, which will be discussed further in Sec. 5.4. Another disadvantage is that the results are not in appropriate units because the argument of the natural logarithm in  $S = -k_B \int d^3 r d^3 v f \ln f$  from Eq. (8) is not dimensionless. This comes about because a term is dropped from Eq. (7), and the dropped term contains information about the units inside the natural log. So, to convert the simulated continuous Boltzmann entropy to real units for comparison to observations or experiments, one must either (a) include the dropped term or (b) choose a reference value of continuous Boltzmann entropy at a particular location and time and present all values as a change in kinetic entropy relative to that reference. This enforces that the quantities have the appropriate units.

## 4. SIMULATIONS

Simulations are carried out using the P3D code (Zeiler et al. 2002), though we expect the diagnostic and analysis would

be possible with any explicit PIC code. The code uses the relativistic Boris particle stepper (Birdsall & Langdon 2004) for the particles and trapezoidal leapfrog (Guzdar et al. 1993) on the electromagnetic fields, with the fields allowed to have a smaller time step than the particles (half as big for our simulations). The divergence of the electric field is cleaned (every 10 particle time steps unless otherwise noted for our simulations) using the multigrid approach (Trottenberg et al. 2000). Boundary conditions in every direction are periodic. The normalization is based on an arbitrary magnetic field strength  $B_0$  and density  $n_0$ . Spatial and temporal scales are normalized to the ion inertial length  $d_i = c/\omega_{pi}$  and the ion cyclotron time  $\Omega_{ci}^{-1}$ , respectively, where  $\omega_{pi} = \sqrt{n_0 e^2 / \epsilon_0 m_i}$  is the ion plasma frequency and  $\Omega_{ci} = eB_0/m_i$  is the ion cyclotron frequency based on  $n_0$  and  $B_0$ . Thus, velocities are normalized to the Alfvén velocity  $v_A = d_i \Omega_{ci}$ . Electric fields are normalized to  $v_A B_0$ . Pressures and temperatures are normalized to  $B_0^2/\mu_0$  and  $mv_A^2/k_B$ , respectively. Entropies are normalized to Boltzmann’s constant  $k_B$ , though see Sec. 3.4 for a discussion of the units of the continuous Boltzmann entropy.

For simplicity in this initial study, we only consider 2D in position space, 3D in velocity space simulations of symmetric anti-parallel magnetic reconnection. The simulation domain is  $L_x \times L_y = 51.2 \times 25.6$ . A double current sheet initial condition is used, with magnetic field given by  $B_x(y) = \{\tanh[(y - 3L_y/4)/w_0] - \tanh[(y - L_y/4)/w_0] + 1\}$ , where  $w_0 = 0.5$  is the initial half-thickness of the current sheet. The initial velocity distribution functions are drifting Maxwellians with temperatures  $T_e = 1/12$  and  $T_i = 5/12$  for electrons and ions, respectively; both temperatures are initially uniform over the whole domain. We use these temperature values so that  $v_{th,e}$  and  $v_{th,i}$  are similar and a common velocity space bin size can be used (see Sec. 3.2). The density is set to balance plasma pressure in the fluid sense, with  $n(y) = \text{sech}^2(y - L_y/4)/w_0 + \text{sech}^2(y - 3L_y/4)/w_0 + n_b$ , where  $n_b = 0.2$  is the background (lobe) density. Unlike the Geospace Environmental Modeling (GEM) magnetic reconnection challenge simulations (Birn et al. 2001), there is only one Maxwellian component in the current sheet. The ion-to-electron mass ratio  $m_i/m_e = 25$  and the speed of light  $c$  is 15. These choices enforce that the plasma is non-relativistic (the speed of light exceeds the thermal and Alfvén speeds), which is appropriate for the non-relativistic treatment of kinetic entropy being considered here.

We use a small enough spatial grid scale and time step to ensure excellent conservation of energy and minimize numerical dissipation. We employ a time step of  $\Delta t = 0.001 \Omega_{ci}^{-1} = 0.025 \Omega_{ce}^{-1} = 0.075 \omega_{pe}^{-1}$ , which is a factor of about 2.67 smaller than what would typically be used for these simulation parameters. The smallest electron Debye length for this simulation (based on the maximum density of  $1 + n_b$ ) is  $\lambda_{De} = 0.018$ . We select a grid scale of  $\Delta x = \Delta y = 0.0125 \approx$

$0.6944 \lambda_{De}$ , again smaller than what is typically used for these simulation parameters to improve energy conservation.

There are a number of parameters that need to be set for the kinetic entropy calculation. These parameters are only for the kinetic entropy diagnostic; they do not influence the rest of the simulation. As discussed in Sec. 3, in order to calculate the combinatorial Boltzmann entropy  $\mathcal{S}$  properly, the number of actual particles per macro-particle  $a$  has to be specified at run time.

We first estimate  $a$  using the method described in Sec. 3.1. For the “base” simulation, the particle weight is proportional to the local density at  $t = 0$ , with a value of  $W = 0.2/1.44$  in the lobe and  $W = 1.2/1.44$  at the center of current sheet. We use  $PPG = 100$  in the base simulation and, as calculated above, a grid scale of  $\Delta x = 0.6944 \lambda_{De}$ . To relate to the actual number of particles, we appeal to the system of interest being simulated. For a simulation representing the plasma in a solar active region, Table 1 gives  $n\lambda_{De}^3 \simeq 1.3 \times 10^7$ , so Eq. (25) gives  $N_{cell} \simeq 4.3 \times 10^6$  actual particles per grid cell. Using  $W = 0.2/1.44$ , Eq. (27) gives  $a = 3.13 \times 10^5$  actual particles per macro-particle. For the plasma sheet in Earth’s magnetotail, Table 1 gives  $n\lambda_{De}^3 \simeq 1.0 \times 10^{13}$ , so assuming the same weight and grid scale gives  $a = 2.5 \times 10^{11}$ . For what we refer to as the “base” simulation, we use  $a = 3.13 \times 10^5$ .

We also need to choose the velocity space bin size  $\Delta v$  and the initial number of macro-particles per grid cell  $PPG$  per species. For each, we must optimize these parameters, which is discussed in detail in Secs. 5.4 - 5.6. For the base simulation, we use  $\Delta v = 1$  and  $PPG = 100$ .

## 5. RESULTS

The layout of this section is as follows. We start with a validation of the implementation of the kinetic entropy diagnostics in the code in Sec. 5.1. The time evolution and conversion of energy and kinetic entropy is discussed in Sec. 5.2. We discuss the position and velocity space entropies in Sec. 5.3. Sections 5.4-5.6 contain results on varying  $a$ ,  $PPG$ , and  $\Delta v$ , respectively. Unless otherwise noted, the results presented here employ the implementation discussed in Sec. 3 on the base simulation described in Sec. 4.

### 5.1. Validation of the Kinetic Entropy Diagnostic

Figure 2(a) shows a 2D plot of the continuous Boltzmann entropy density  $s_e(\vec{r})$  from Eq. (9) at time  $t = 0$  for electrons; results for ions are analogous. The center of the plot is shifted to the position of the X-line  $(x_0, y_0)$  of the top current sheet at  $y_0 = 3L_y/4$ . Panel (b) shows the electron density  $n_e$  at the same time. The structure of  $s_e$  is strongly determined by the density, as expected from Eq. (10) for Maxwellian distributions such as those at the initial conditions of the present simulations. Panels (c) and (d) show similar plots, but for  $t = 41$ , showing a similar relationship between kinetic entropy and

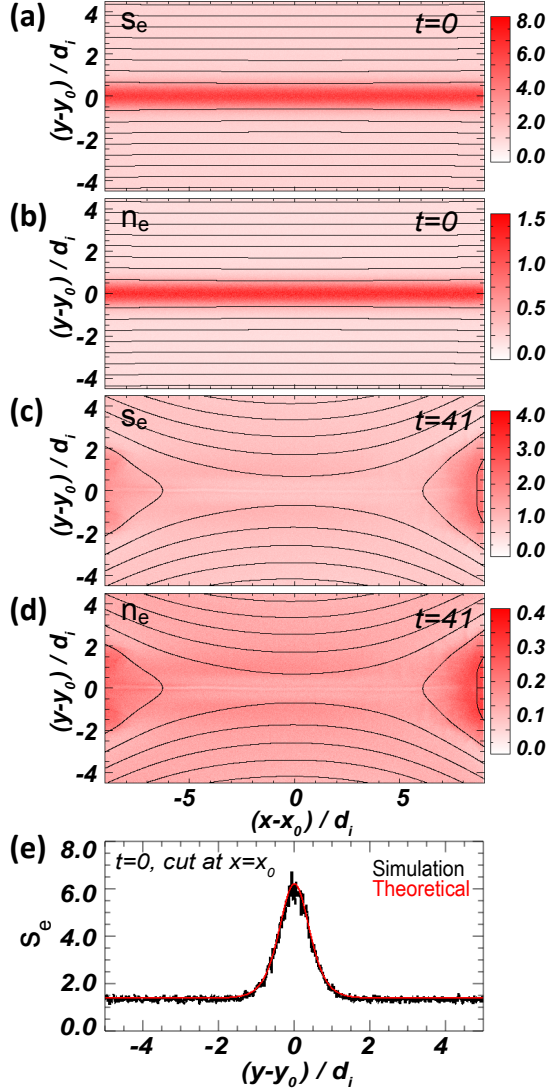


**Figure 2.** 2D plots, zoomed in near the reconnection X-line at  $(x_0, y_0)$  of (a) electron kinetic entropy density  $s_e$  and (b) electron density  $n_e$  at time  $t = 0$ . (c) and (d) are the same except at  $t = 41$ . (e) A vertical cut of  $s_e$  through the X-line (black) at  $t = 0$ , with the theoretical prediction (red) overplotted.

density even though distribution functions are no longer all Maxwellian at this time.

The initial distribution functions for this simulation are drifting Maxwellians, so we can validate the implementation of the diagnostic by comparing the calculated  $s_e$  with the analytic calculation in Eq. (10). In the upstream region where the density is 0.2, Eq. (10) predicts a value (in normalized code units) of  $(3/2)(0.2)[1 + \ln(2\pi(1/12)/(0.04 \times 0.2^{2/3}))] = 1.39$ ; in the center of the sheet where the density is 1.2 the analytic prediction is 6.21. Panel (e) shows a vertical cut of the continuous Boltzmann entropy density at  $t = 0$  in black, with the analytical prediction overplotted as the red line, revealing excellent agreement of the theory and simulations. In Sec. 5.4,

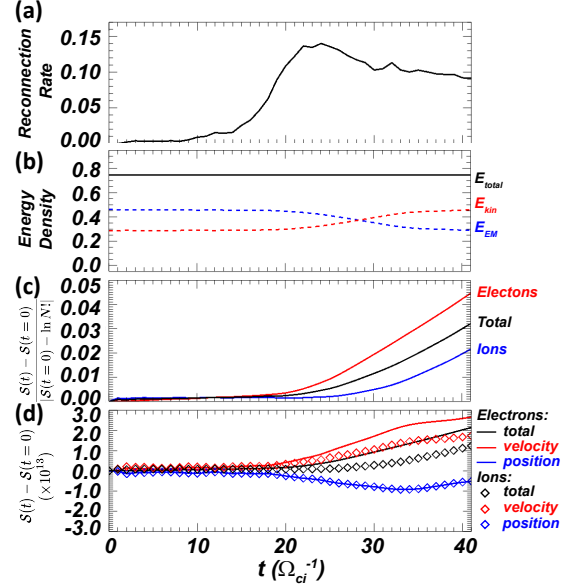


**Figure 3.** Time histories from the base simulation of the following quantities: (a) reconnection rate, (b) total energy density  $E_{total}$  (black solid line), total kinetic energy density  $E_{kin}$  (red dashed line), and electromagnetic energy density  $E_{EM}$  (blue dashed line), (c) relative change of the non-constant term in the combinatorial Boltzmann entropy  $\mathcal{S}(t)$  in Eq. (4) for electrons (red), ions (blue), and total (black), (d) deviation from its initial value of velocity space entropy  $\mathcal{S}_{velocity}$  (red), position space entropy  $\mathcal{S}_{position}$  (blue), and total combinatorial Boltzmann  $\mathcal{S}$  (black) for electrons (solid curves) and ions (diamonds).

we confirm that the combinatorial  $\mathcal{S}$  and continuous  $S$  Boltzmann entropies are in agreement, as they should be. We conclude that the kinetic entropy diagnostics implemented here successfully determine the kinetic entropy.

## 5.2. Energy and Kinetic Entropy Conservation and Conversion

A principal diagnostic of momentum-conserving PIC codes is the conservation of total (particle plus electromagnetic) energy. Departures from perfect conservation occur only as a result of numerical effects including finite time step, finite grid scale, and noise introduced by having a finite number of macro-particles. In a collisionless PIC code, as is the case for the one employed in this study, kinetic entropy should also be conserved (Bellan 2008), with departures from perfect conservation again only arising due to numerical effects. Here, we investigate energy and kinetic entropy conservation in our base simulation.

The time evolution of the system is shown using the reconnection rate as a function of time  $t$  in Fig. 3(a). The reconnection rate is the time rate of change of magnetic flux between the X-line and O-line, identified at each time  $t$  using the saddle and extremum of the magnetic flux function  $\psi(\vec{r})$  defined by  $\vec{B} = \hat{z} \times \nabla \psi$ , where  $\vec{B}$  is the magnetic field. As is typical

in 2D PIC simulations in periodic domains, the reconnection rate starts to grow from zero (visibly at  $t \approx 10$ ), reaches a peak (at  $t \approx 21.5$ ), and then falls back down to a reasonably steady state (for  $t > 34$ ).

Figure 3(b) shows total energy density  $E_{total}$  (black solid curve), total kinetic energy density  $E_{kin}$  (red dashed curve) including both bulk and thermal kinetic contributions, and total electromagnetic energy density  $E_{EM}$  (blue dashed curve), as a function of time  $t$  for the base simulation. The total energy only increases 0.24% by  $t = 41$ ; this is excellent total energy conservation. This is the result of our intentional use of a small time step and grid scale. The expected conversion of electromagnetic energy to kinetic energy during the reconnection process (starting in earnest at about  $t = 20$ ) is also seen in the time histories.

Now, we investigate how the kinetic entropy changes in time during the simulation, including both relative and absolute changes in kinetic entropy since both provide useful insights. For the relative change of the combinatorial Boltzmann entropy  $\mathcal{S}$  in Eq. (4), it is important to note that  $[\mathcal{S}(t) - \mathcal{S}(t=0)]/\mathcal{S}(t=0)$  is not a meaningful measure of the kinetic entropy change because the first term  $k_B \ln N!$  is a constant; only the second term can vary. Therefore, one should normalize to only the part of the kinetic entropy that can change,  $\mathcal{S}(t=0) - k_B \ln N!$ .

Figure 3(c) shows the change of the combinatorial Boltzmann entropy in time from Eq. (4) normalized to  $\mathcal{S}(t=0) - k_B \ln N!$  for the base simulation, with values for electrons in red, ions in blue, and their total in black. The relative changes are about 4.5%, 2.1% and 3.2% by  $t=41$  for electrons, ions, and total, respectively. In general, the kinetic entropies are conserved reasonably well, given that reconnection occurs and there is a conversion of nearly one-third of the electromagnetic energy into particle kinetic energy. Interestingly, the kinetic entropy due to numerical effects is monotonically increasing. If the code had physical collisions, one would expect the kinetic entropy would monotonically increase. We find that the numerical effects, in this sense, mimic physical collisions.

The absolute change to the kinetic entropy is now used to study the partition between electrons and ions. Figure 3(d) shows the total combinatorial Boltzmann entropy  $\mathcal{S}$  (in black) for electrons (solid line) and ions (diamonds) as a function of time  $t$ . Each has its initial value subtracted so that the plotted values are the change relative to the initial time. Notice the change in the absolute kinetic entropies are quite large, at the  $10^{13}$  level in code units (corresponding to the  $10^{-10}$  level in units of J/K). This ostensibly large number is a result of the number of actual particles represented in the simulation being large. In particular, the base simulation has 100 PPG and  $4096 \times 2048$  cells, for a total of 838,860,800 macro-particles. With  $a = 3.13 \times 10^5$ , the total number of

particles represented is  $N = 2.6 \times 10^{14}$ . The first term in the kinetic entropy in Eq. (5) is  $\ln N!$ , which is approximately  $8.5 \times 10^{15}$ . This sets the scale of kinetic entropies for this system; we find the total kinetic entropies after the subtraction due to the second term in Eq. (5) are at the  $10^{14}$  level, and the change in kinetic entropy in time is at the  $10^{13}$  level, as seen in Fig. 3(d).

Comparing the total kinetic entropies for each individual species, we see that both increase in time as might be expected, but the electrons gain more than the ions in an absolute sense. This is very reasonable, as numerical effects arising at small scales are expected to disproportionately affect electrons.

### 5.3. Position and Velocity Space Entropies

We now discuss the position and velocity space entropies discussed in Sec. 2.2. The two terms are calculated from Eqs. (12) and (13) using the combinatorial Boltzmann entropy  $\mathcal{S}$ . Their evolution is shown in Fig. 3(d), with position space entropies in blue and velocity space entropies in red with electrons given by the solid lines and ions by the diamonds. First, we note that the position space entropy is essentially the same for electrons and ions. This is consistent with expectations as a result of quasi-neutrality of the plasma.

The velocity space entropy increases for both electrons and ions, a result of a temperature increase of both species due to the reconnection process, as expected from Sec. 2.2. The increase in velocity space entropy is associated with a decrease in the position space entropy. If kinetic entropy is perfectly conserved, as the governing equations would have in this closed system, then any increase in velocity space entropy would necessarily be offset by a decrease in position space entropy. In the simulation, total kinetic entropy is not conserved perfectly, but we still observe a decrease in position space entropy for both electrons and ions. Physically, this decrease is associated with the enhanced density in the island as reconnection proceeds and upstream plasma is compressed. Compression leads to more particles in some phase space bins, lowering the position space entropy as discussed in Sec. 2.2.

This explanation is predicated on the notion that the temperature increase is physical rather than numerical, so we investigate this here. The increase of total entropy due to numerical effects is less than 5%, as discussed in Sec. 5.2. One might expect the thermal energy change from numerical effects  $\Delta E_{th, numerical}$  to scale like  $Q_{numerical} \simeq T \Delta S_{numerical}$  from the first law of thermodynamics, so  $\Delta E_{th, numerical}$  would be at the 5% level. However, in the simulation, the thermal energy gain for electrons and ions are 103% and 77%, respectively. This implies that physical heating is much more significant than the contribution due to numerical effects.

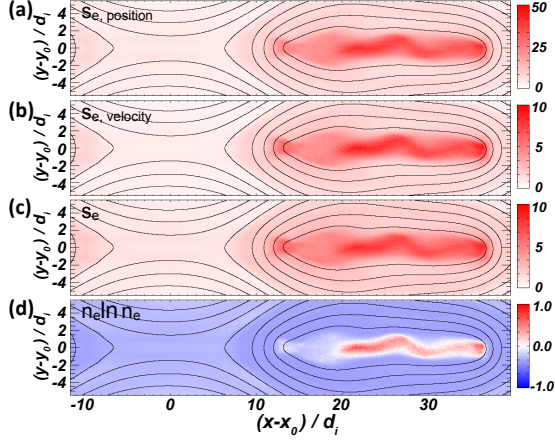


**Figure 4.** 2D plots of various kinetic entropies at time  $t = 41$  for electrons: (a) position space entropy density  $s_{e,\text{position}}(\vec{r})$ , (b) velocity space entropy density  $s_{e,\text{velocity}}(\vec{r})$ , (c) continuous Boltzmann entropy density  $s_e(\vec{r})$ , and (d) the  $n_e(\vec{r}) \ln n_e(\vec{r})$  term that arises in the calculation of  $s_{e,\text{position}}$ .

This result also underscores a point about temperature and entropy that is important to take into account in laboratory and satellite measurements of kinetic entropy. In this simulation, there is a significant increase in thermal energy, but only a small change in kinetic entropy. This shows that a temperature increase is not necessarily associated with an increase in total kinetic entropy.

To get a sense for what the different kinetic entropies look like as a function of space, Fig. 4 includes plots of (a) position space entropy density  $s_{e,\text{position}}(\vec{r})$  [from Eq. (22)], (b) velocity space entropy density  $s_{e,\text{velocity}}(\vec{r})$  [from Eq. (24)], (c) continuous Boltzmann entropy density  $s_e(\vec{r})$  [from Eq. (9)], and (d)  $n_e(\vec{r}) \ln n_e(\vec{r})$ , a term that arises in the position space entropy. These plots are all for electrons and are taken at  $t = 41$ , showing the whole domain in  $x$  and are zoomed in to the upper current sheet in  $y$ . The region of increased velocity space entropy is mostly within the magnetic island, which is where the plasma is compressed. For the parameters in the base simulation, the difference between  $s_e(\vec{r})$  and  $s_{e,\text{velocity}}(\vec{r})$  is at about the 10% level.

#### 5.4. Importance of Including Actual Particles Per Macro-particle for the Combinatorial Boltzmann Entropy

As discussed in Sec. 3.1, to calculate the combinatorial Boltzmann entropy  $\mathcal{S}$ , one must include the number of actual particles per macro-particle  $a$ . Here, we show this is the case in the simulations. Furthermore, since the combinatorial  $\mathcal{S}$  and continuous  $S$  Boltzmann entropies should be nearly identical for a large number of particles, we can use this as a further test of the implementation of the diagnostics.

We perform three simulations that are identical except for the use of different values of  $a$ . An  $a = 1$  case has each macro-

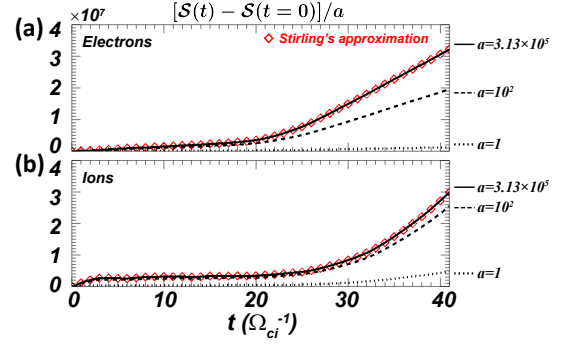


**Figure 5.** Combinatorial Boltzmann entropy deviations from their initial value normalized to  $a$ , i.e.,  $[\mathcal{S}(t) - \mathcal{S}(t=0)]/a$  for (a) electrons and (b) ions. Solid, dashed, and dotted lines are for  $a = 3.13 \times 10^5$ ,  $10^2$  and 1, respectively. The red diamond symbols indicate the value for the continuous Boltzmann entropy  $S$  from Eq. (8).

particle representing a single particle, and we also use values of  $a = 100$  and the base simulation using  $a = 3.13 \times 10^5$ . Figure 5 contains results for the time evolution of the total combinatorial Boltzmann entropy  $\mathcal{S}(t)$  integrated over the entire computational domain, shown as a difference from its initial value  $\mathcal{S}(t=0)$  and divided by  $a$ , for the three simulations. Panel (a) is for electrons and panel (b) is for ions. The reason to divide by  $a$  is that we know from Eq. (30) that the continuous Boltzmann entropy  $S$  is directly proportional to  $a$  in the limit of large number of particles, so dividing by  $a$  allows us to directly compare simulations that use different values of  $a$ . The red diamonds show the corresponding value of the kinetic entropy from Eq. (8), which follows after employing the Stirling approximation. First, we note that there is excellent agreement in the large  $a$  simulation between the combinatorial  $\mathcal{S}$  and continuous  $S$  Boltzmann entropies as there should be, which provides additional evidence for the proper implementation of the diagnostic. For the  $a = 100$  case, a significant difference between the two is observed, especially for the electrons. For the  $a = 1$  case, the difference is at least an order of magnitude. The results show that if  $a$  is not included, or is too low, the combinatorial Boltzmann entropy  $\mathcal{S}$  does not agree with the continuous Boltzmann entropy  $S$ .

To be more specific, a typical maximum value of macro-particles in a phase space bin is approximately 3 in the base simulation. Taking into account the particle weight of  $W = 0.2/1.44$ , analogous to the discussion in Sec. 3.1 leading to Eq. (26), for a simulation with  $a = 100$  implies that there are a maximum of about  $3 \times (0.2/1.44) \times 100 \simeq 40$  actual particles in any phase space bin. The error due to the Stirling approximation for an argument of 40 is about 1%. While this is reasonably good, it represents the minimum error in any cell. Bins with fewer particles contribute higher errors (4 actual particles has a 15% error), leading to the larger errors approaching 30% we see for the  $a = 100$  simulation. For

$a = 3.13 \times 10^5$ , the maximum particles per cell is 130,000, for which the error introduced by the Stirling approximation is exceedingly small ( $3 \times 10^{-4}\%$ ). This motivates the approximate level of disagreement for the  $a = 100$  simulation and why the larger  $a$  gives good agreement. We note that there are a number of physical systems for which  $a$  would be of order 100 for  $PPG$  near 100 and a weight of  $W = 1$ , such as Earth's ionosphere, the MRX reconnection experiment, and high energy density laser plasmas, as seen in Table 1, so there are physical systems for which errors could be introduced by using the Stirling approximation.

### 5.5. Dependence on Macro-particles Per Grid Cell ( $PPG$ )

The limited number of macro-particles in PIC simulations leads to a worse statistical representation of phase space than in the actual system being simulated. Here, we investigate how this impacts the calculation of kinetic entropy by comparing simulations with different numbers of macro-particles per grid cell, keeping the actual number of particles fixed by keeping  $a$  times  $PPG$  constant. This ensures there are a sufficient number of particles to avoid accuracy issues as discussed in Sec. 5.4. We carry out simulations with  $PPG$  of 1, 25, 50, and the base simulation of 100. For  $PPG = 50, 25$ , and 1, we use  $a = 6.27 \times 10^5, 1.25 \times 10^6$ , and  $3.13 \times 10^7$ , respectively. The reasons we include a case with  $PPG=1$  are (1) some studies have used low  $PPG$  in PIC simulations and (2) we can test what happens to the kinetic entropy calculation when the statistics are poor.

Some extra details for the  $PPG = 1$  case are warranted. Since numerical PIC noise is expected to be significant, we start by performing a simulation with the same divergence cleaning frequency as the other simulations (every 10 particle time steps). We find the time history of the reconnection rate is very different than the higher  $PPG$  simulations due to the numerical noise and relatively bad energy conservation. Then, we perform another simulation with divergence cleaning at every time step, which reduces the impact of the noise. The total energy change in this simulation is 7.3%, and the reconnection rate evolution is similar to the higher  $PPG$  simulations. We find the magnitude of the kinetic entropy change is similar to the  $PPG = 1$  case with less frequent divergence cleaning. Consequently, we use the  $PPG = 1$  simulation with the higher cadence divergence cleaning in what follows.

Figure 6(a) shows the reconnection rate as a function of time for the four simulations, with the colors defined in the plot and caption. The plot clearly shows that the reconnection rate is quite insensitive to  $PPG$ , even for a value of  $PPG = 1$  (with additional divergence cleaning). That the reconnection rate can be accurately simulated in PIC simulations with few particles has been previously noted in astrophysical PIC simulation studies of reconnection (Sironi & Spitkovsky 2014; Sironi et al. 2016; Ball et al. 2018).

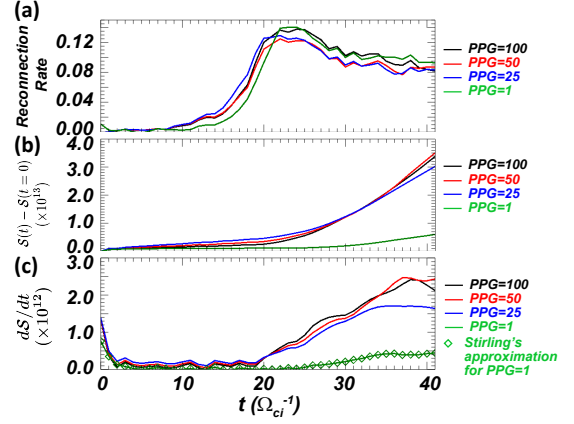


**Figure 6.** (a) Reconnection rate, (b) deviation of the total combinatorial Boltzmann entropy  $S$  from its initial value, and (c) time rate of change of the total combinatorial Boltzmann entropy  $S$  for simulations with different  $PPG$  of 100 (black), 50 (red), 25 (blue), and 1 (green). In (c), the diamonds show the corresponding value using the continuous Boltzmann entropy  $S$  instead of the combinatorial Boltzmann entropy  $S$  for the  $PPG=1$  case to confirm it is calculated properly.

Panel (b) shows the deviation of the combinatorial Boltzmann entropy  $S$  from its initial value for the four simulations with different  $PPG$ . The  $PPG=1$  case deviates from the others significantly, but the results of the other three cases are similar. In order to examine the differences among  $PPG=100, 50$  and  $25$ , we further plot the time rate of change of the combinatorial Boltzmann entropy  $dS/dt$  in panel (c). The results for the  $PPG = 50$  and  $100$  cases are quite similar. This suggests that these numbers for  $PPG$  are sufficient to give a relatively stable regime of the kinetic entropy calculation for our simulations.

In contrast, the  $PPG = 25$  results differ from the higher  $PPG$  results, showing that adverse numerical effects from the worse particle statistics take place, especially late in time after reconnection occurs. It is even more dramatic for  $PPG = 1$ , where there is a large discrepancy approaching an order of magnitude. This suggests that even though a  $PPG$  of 1 can be made to reasonably produce the reconnection rate, one must proceed with caution on matters related to kinetic entropy, including effects such as particle acceleration and plasma heating. A convergence test of kinetic entropy and the effect of small  $PPG$  on energization, heating, and energy partitioning would be useful in testing such simulations.

It may seem counter-intuitive that the kinetic entropy decreases with fewer  $PPG$ . The reason is that the smaller number of macro-particles implies that a smaller number of microstates can be produced through their permutation, which lowers the kinetic entropy. A 2D plot of the kinetic entropy density of the  $PPG = 1$  simulation (not shown) is very similar to the density, as expected, but the departure of the distribution from a Maxwellian has very large noise which swamps

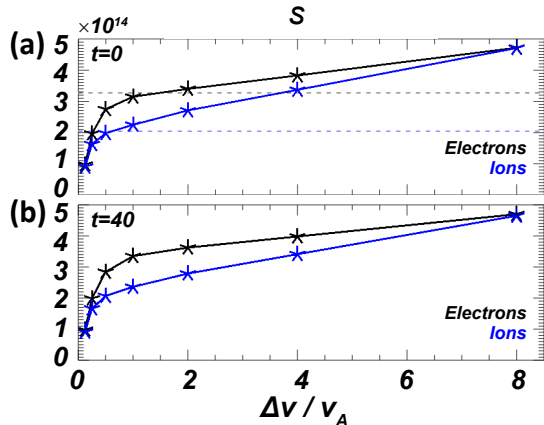


**Figure 7.** Continuous Boltzmann entropy  $S$  for electrons (black) and ions (blue) in seven simulations with  $\Delta v/v_A = 0.125, 0.25, 0.5, 1.0, 2.0, 4.0, 8.0$  (a) at  $t = 0$  and (b) at  $t = 40$ . The dashed lines in (a) indicate the analytical values at  $t = 0$  for electrons (black) and ions (blue).

out all other structures (since a Maxwellian is not well described by a single macro-particle). This further suggests that a sufficiently large *PPG* is necessary to get a reasonable description of kinetic entropy.

### 5.6. Dependence on $\Delta v$

While the kinetic entropy should not depend on grid scale for the continuous form in Eq. (8), the discrete form in Eq. (7) is required for implementation in PIC and therefore is dependent on the grid scale. Here, we discuss how to choose the size of the velocity space bin size  $\Delta v$ . The dependence on spatial grid size could be determined using the same approach, but this is left for future work. We choose the optimal  $\Delta v$  by comparing simulation results for different  $\Delta v$  to analytical results for known Maxwellian distributions at  $t = 0$  in the base simulation.

We show results from multiple simulations using velocity bin sizes  $\Delta v$  of 0.125, 0.25, 0.5, 1.0, 2.0, 4.0, and 8.0 relative to the ion Alfvén speed  $v_A$ . Figure 7 shows the continuous Boltzmann entropy  $S$  at (a) the initial time  $t = 0$  and (b) late time  $t = 40$  for both electrons (black) and ions (blue) as a function of the velocity space grid scale  $\Delta v$  normalized to the ion Alfvén speed  $v_A$ . As expected, the continuous Boltzmann entropy  $S$  of both species increases with  $\Delta v$  for sufficiently large values. Below  $\Delta v/v_A$  of about 0.5 or 1, the variation strongly depends on  $\Delta v$ .

Also in panel (a) are black and blue horizontal dashed lines corresponding to the analytical prediction of the continuous Boltzmann entropy of electrons and ions, respectively, for the initial conditions from the spatial integral of Eq. (10). By inspection, we see that the numerically calculated value of electron kinetic entropy agrees well with the analytical value for a velocity grid scale just over  $1 v_A$ . This suggests an ap-

propriate value to use for the velocity space grid of electrons. Similarly, the ion kinetic entropy agrees with the analytical value for a velocity grid just under  $1 v_A$ . These two results motivated our choice of a grid scale of  $\Delta v = 1 v_A$ , which is  $\approx 0.69 v_{th,e}$  in terms of the initial electron thermal speed  $v_{th,e}$  for this simulation. That this is slightly less than the electron thermal speed is consistent with expectations, as discussed in Sec. 3.2. Note, for both electrons and ions, the velocity grid scale that gives best agreement with the analytical calculation is near the species thermal speed ( $1.44 v_A$  for electrons,  $0.65 v_A$  for ions). Also, the base simulation used the same velocity space grid scale for ions and electrons; this is not a requirement and could be relaxed.

## 6. DISCUSSION AND CONCLUSION

### 6.1. Summary

This manuscript presents a study of how to implement two forms of the kinetic entropy into fully kinetic particle-in-cell simulations and how to use these quantities to diagnose the physical system. The two forms are the combinatorial Boltzmann entropy  $S = k_B \ln \Omega$  and the continuous Boltzmann entropy  $S = -k_B \int d^3 r d^3 v f \ln f$ . These forms of kinetic entropy, can be decomposed into a sum of two terms describing the kinetic entropy in position space and velocity space separately.

We then discuss how to implement the diagnostic into PIC simulations, including considerations such as the optimal size of the velocity space grid scale, the number of macro-particles per grid cell, and the number of actual particles per macro-particle. We compare and contrast the merits of each of the two measures of kinetic entropy.

Then, we validate the implementation using two-dimensional in position space, three-dimensional in velocity space collisionless PIC simulations of anti-parallel symmetric magnetic reconnection. The initial conditions contain only drifting Maxwellian distributions which has an analytical solution for the kinetic entropy. This allows for a careful validation of the implementation and provides an avenue for optimizing the velocity space grid size. Finally, we discuss the interpretation of the results and how to extract physical understanding from the kinetic entropy.

The results of the present study include the following:

1. The “base” simulation with very low  $\Delta t$  demonstrates good conservation of the total kinetic entropy (to 3.2%). The increase in kinetic entropy is purely numerical, increases monotonically as would be expected for physical collisions, and increases faster when reconnection proceeds.
2. Electrons and ions show different kinetic entropy production rates, with electrons gaining more than ions in the base simulation because their dynamics occurs at

smaller scales and therefore are disproportionately impacted by numerical effects.

3. Although the total kinetic entropy is nearly conserved, the position and velocity space entropies  $S_{\text{position}}$  and  $S_{\text{velocity}}$  vary noticeably in time. For both electrons and ions,  $S_{\text{position}}$  decreases in time (for most of the simulation), while the  $S_{\text{velocity}}$  increases in time. This is physically related to the electrons and ions getting heated during reconnection (increasing their velocity space entropy) and getting compressed (decreasing their position space entropy).
4. Calculating the combinatorial Boltzmann entropy  $\mathcal{S}$  requires specifying the number of actual particles per macro-particle  $a$  for the calculation, while the continuous Boltzmann entropy only needs this quantity to convert to real units for comparison with observations or experiments.
5. We show how to choose a velocity space bin size and the number of macro-particles per grid cell  $PPG$ . For these simulations, a bin size that is close to the electron thermal speed is a good size, and we need at least 50  $PPG$  to get reliable kinetic entropy values for our choice of time step and spatial grid scale. The minimum  $PPG$  that is sufficient to reliably calculate the kinetic entropy likely depends on these quantities.

Our study shows that kinetic entropy can serve as a diagnostic of the fidelity of a collisionless PIC code, alongside the often used energy, but also can give key physical insights about the dynamics of a system. The diagnostic developed here should be applicable to any explicit PIC simulation, which should make it useful in many astrophysical, heliospheric, and planetary processes including magnetic reconnection, plasma turbulence, and collisionless shocks.

## 6.2. Numerical Insights and Applications

This work provides a number of numerical insights that are important for applying the kinetic entropy diagnostic for applications. Kinetic entropy in a PIC simulation is sensitive to the phase space bin size, both in position and velocity space. This is because the calculation is discretized on a finite grid. Comparisons between different times in a given simulation, between two different simulations, and between simulations and data should be done with a fixed position and velocity space grid scale to the extent possible.

An interesting result is that one needs to be careful to ensure the bins in phase space have a large number of (actual) particles to obtain accurate kinetic entropy values. Stirling's approximation is good to within 1% when the number of actual particles in a bin is 40 but has 15% error for 4 actual particles in a bin. Thus, computational and observational studies

alike should monitor the number of particles per phase space bin. It is possible in either setting to have insufficient counts to render the Stirling approximation valid. In such cases, the combinatorial Boltzmann entropy  $\mathcal{S}$  in Eq. (1) is needed over the continuous Boltzmann entropy  $S$  in Eq. (8). As discussed in Sec. 5.4, this is the case for some important plasma settings, potentially including laboratory experiments, Earth's ionosphere, and laser plasmas.

We point out the importance of ensuring a stable regime of the kinetic entropy with the number of numerical macro-particles per grid cell  $PPG$ . For the base simulation with small time step and well-resolved grid, we find we need at least 50 for  $PPG$  to have a stable regime of the kinetic entropy. There have been a number of studies, especially in the plasma astrophysics community, with smaller  $PPG$  including as low as 1-4 (Sironi & Spitkovsky 2014; Sironi et al. 2016; Ball et al. 2018). We confirm their results that one can get a reasonable reconnection rate in such systems, but for our code the low  $PPG$  is insufficient to get a proper kinetic entropy. The Ball et al. (2018) study tested convergence of particle energy spectra with  $PPG$  of 4 and 16; it would be interesting to also check stability of the kinetic entropy diagnostic. We suggest that using kinetic entropy to test for stability for low  $PPG$  simulations is a useful technique which is potentially important for studies of particle acceleration and plasma heating in reconnection, turbulence, and shocks.

One challenge for applications is that the conservation of kinetic entropy in ideal (collisionless) systems is only valid for closed, isolated systems. This can easily be accomplished in idealized simulations, but it is unlikely to be the case in naturally occurring systems. The expectation of this line of research is that the dissipation physics can be studied using idealized simulations, and then the insights obtained from the simulations can be compared to real systems. This is already being carried out with data from MMS and will be the subject of future publications.

Another challenge is that typically the continuous Boltzmann entropy density  $s = -\int d^3v f \ln f$  is mostly proportional to the number density, so a plot of kinetic entropy density by itself is unlikely to reveal any new insights. We will demonstrate in a follow up study (Liang et al. in prep.) that kinetic entropy can be useful for identifying non-Maxwellian distributions for electrons and ions and furthermore that the kinetic entropy can be used to estimate the effective numerical collisionality of a collisionless PIC code.

The initial implementation of the kinetic entropy diagnostic has many ways to be improved, which we outline here. First, our treatment is non-relativistic, but the PIC code in use and many natural systems relevant to study with this tool are relativistic (Kaniadakis 2009). In addition, comparisons to implicit PIC simulations (which can employ much larger spatial grids and time steps) and Vlasov simulations (which



have no PIC noise) would be interesting. More in depth studies into the dependence of the kinetic entropy diagnostic on spatial grid scale and time step would be useful, along with higher macro-particles per grid cell *PPG*. Our work used only the linear shape function; it would be interesting to test other shape functions. It would also be interesting to examine kinetic entropy in PIC simulations with open boundary conditions. The present simulations are 2D in position space and 3D in velocity space; simulations that are 3D in both position and velocity space should be carried out. Most importantly, this work employs only collisionless PIC simulations, which means that any dissipation (*i.e.*, any increase of total kinetic entropy) that occurs is through numerical effects. Thus, we are unable to address physical mechanisms for dissipation in the present study. Using a collisional PIC code would allow for an investigation of the physical mechanisms of dissipation with the kinetic entropy diagnostic.

There are also numerous physics topics that are important for future work. Future work should also address plasma tur-

bulence and collisionless shocks. Generalizations to other forms of entropy, such as the Tsallis entropy which describes long-range interactions and contains memory effects (Tsallis 1988), should also be undertaken. Whether chaotic behavior is sufficient to produce an entropy increase should also be the subject of future work. It is important to see if numerical kinetic entropy production can impact other physical processes like particle acceleration and heating.

We acknowledge helpful conversations with A. Glocer, H. Hietala, W. Paterson, S. Schwartz, and E. G. Zweibel. We thank J. Burch for motivation for this project. Support from NSF Grants AGS-1460037, AGS-1602769, and PHY-1704428 and NASA Grant NNX16AG76G is gratefully acknowledged. This research uses resources of the National Energy Research Scientific Computing Center (NERSC), a DOE Office of Science User Facility supported by the Office of Science of the U.S. Department of Energy under Contract No. DE-AC02-05CH11231.

## REFERENCES

- Arfken, G. B. & Weber, H. J. 1995, *Mathematical Methods for Physicists*, 4th edn. (Academic Press)
- Ashour-Abdalla, M., Lapenta, G., Walker, R., El-Alaoui, M., Liang, H., Zhou, M., Berchem, J., & Goldstein, M. L. 2016, *Geophysical Research Letters*, 43, 6005
- Balasis, G., Daglis, I. A., Papadimitriou, C., Kalimeri, M., Anastasiadis, A., & Eftaxias, K. 2009, *J. Geophys. Res.*, 114, A00D06
- Ball, D., Sironi, L., & Özel, F. 2018, arXiv preprint arXiv:1803.05556
- Beall, J. H. 2014, *Acta Polytechnica CTU Proceedings*, 1, 259
- Bellan, P. M. 2008, *Fundamentals of Plasma Physics* (Cambridge University Press)
- Birdsall, C. K. & Langdon, A. B. 2004, *Plasma Physics via Computer Simulation* (Taylor & Francis)
- Birn, J., Drake, J. F., Shay, M. A., Rogers, B. N., Denton, R. E., Hesse, M., Kuznetsova, M., Ma, Z. W., Bhattacharjee, A., Otto, A., & Pritchett, P. L. 2001, *J. Geophys. Res.*, 106, 3715
- Birn, J., Galsgaard, K., Hesse, M., Hoshino, M., Huba, J., Lapenta, G., Pritchett, P., Schindler, K., Yin, L., Büchner, J., Neukirch, T., & Priest, E. 2005, *Geophys. Res. Lett.*, 32
- Birn, J., Hesse, M., & Schindler, K. 2006, *Phys. Plasmas*, 13, 092117
- Birn, J., Hesse, M., Schindler, K., & Zaharia, S. 2009, *J. Geophys. Res.*, 114, A00D03
- Boltzmann, L. 1877, *Wiener Berichte*, 76, 373, in (Boltzmann 1909) Vol. II, paper 42.
- Borovsky, J. E., Thomsen, M. F., Elphic, R. C., Cayton, T. E., & McComas, D. J. 1998, *J. Geophys. Res.*, 103, 20,297
- Burch, J. L., Moore, T. E., Torbert, R. B., & Giles, B. L. 2016a, *Space Sci. Rev.*, 199, 5
- Burch, J. L., Torbert, R. B., Phan, T. D., Chen, L.-J., Moore, T. E., Ergun, R. E., Eastwood, J. P., Gershman, D. J., Cassak, P. A., Argall, M. R., Wang, S., Hesse, M., Pollock, C. J., Giles, B. L., Nakamura, R., Mauk, B. H., Fuselier, S. A., Russell, C. T., Strangeway, R. J., Drake, J. F., Shay, M. A., Khotyaintsev, Y. V., Lindqvist, P.-A., Marklund, G., Wilder, F. D., Young, D. T., Torkar, K., Goldstein, J., Dorelli, J. C., Avano, L. A., Oka, M., Baker, D. N., Jaynes, A. N., Goodrich, K. A., Cohen, I. J., Turner, D. L., Fennell, J. F., Blake, J. B., Clemmons, J., Goldman, M., Newman, D., Petrinec, S. M., Trattner, K. J., Lavraud, B., Reiff, P. H., Baumjohann, W., Magnes, W., Steller, M., Lewis, W., Saito, Y., Coffey, V., & Chandler, M. 2016b, *Science*, 352, 6290
- Cassak, P. A. 2016, *Space Weather*, 14, 186
- Cerri, S. S., Kunz, M. W., & Califano, F. 2018, *Ap. J.*, 856, L13
- Chen, L.-J., Wang, S., Wilson, L. B., Schwartz, S., Bessho, N., Moore, T., Gershman, D., Giles, B., Malaspina, D., Wilder, F. D., Ergun, R. E., Hesse, M., Lai, H., Russell, C., Strangeway, R., Torbert, R. B., F-Vinas, A., Burch, J., Lee, S., Pollock, C., Dorelli, J., Paterson, W., Ahmadi, N., Goodrich, K., Lavraud, B., Le Contel, O., Khotyaintsev, Y. V., Lindqvist, P.-A., Boardsen, S., Wei, H., Le, A., & Avano, L. 2018, *Phys. Rev. Lett.*, 120, 225101
- Cranmer, S. R. 2002, *Space Sci. Rev.*, 101, 229

- Draine, B. T. & McKee, C. F. 1993, *Annual review of astronomy and astrophysics*, 31, 373
- Drake, J. F., Swisdak, M., Schoeffler, K. M., Rogers, B. N., & Kobayashi, S. 2006, *Geophys. Res. Lett.*, 33, L13105
- Ensslin, T. A., Biermann, P. L., Klein, U., & Kohle, S. 1998, *Astron. Astrophys.*, 332, 395
- Erickson, G. M. & Wolf, R. A. 1980, *Geophys. Res. Lett.*, 7, 897
- Eyink, G. L. 2018, arXiv preprint arXiv:1803.03691
- Frigg, R. & Werndl, C. 2011, in *Probabilities in Physics*, ed. C. Beisbart & S. Hartmann (Oxford University Press), 115
- Gaensler, B. M. & Slane, P. O. 2006, *Ann. Rev. Astron. Astrophys.*, 44, 17
- Goldstein, S. & Lebowitz, J. L. 2004, *Physica D*, 193, 53
- Gosling, J. T. *Encyclopedia of the Solar Wind* (Elsevier)
- Guo, X., Sironi, L., & Narayan, R. 2017, *The Astrophysical Journal*, 851, 134
- . 2018, *The Astrophysical Journal*, 858, 95
- Guzdar, P. N., Drake, J. F., McCarthy, D., Hassam, A. B., & Liu, C. S. 1993, *Phys. Fluids B*, 5, 3712
- Hammett, G. W. & Perkins, F. W. 1990, *Phys. Rev. Lett.*, 64, 3019
- Hesse, M., Chen, L. J., Liu, Y.-H., Bessho, N., & Burch, J. L. 2017, *Phys. Rev. Lett.*, 118, 145101
- Hesse, M., Neukirch, T., Schindler, K., Kuznetsova, M., & Zenitani, S. 2011, *Space Sci. Rev.*, 160, 3
- Hesse, M., Zenitani, S., Kuznetsova, M., & Klimas, A. 2009, *Phys. Plasmas*, 16, 102106
- Howes, G. G. 2018, *Phys. Plasmas*, 25, 055501
- Howes, G. G., Cowley, S. C., Dorland, W., Hammett, G. W., Quataert, E., & Schekochihin, A. A. 2006, *The Astrophysical Journal*, 651, 590
- Jaynes, E. T. *Information Theory and Statistical Mechanics*, Vol. Statistical physics (New York: Benjamin), 219, in *Brandeis University Summer Institute Lectures in Theoretical Physics / 1962 lectures*, edited by K. W. Ford
- Ji, H. & Daughton, W. 2011, *Phys. Plasmas*, 18, 111207
- Johnson, J. R. & Wing, S. 2009, *J. Geophys. Res.*, 114, A00D08
- Kadanoff, L. P. 2014, arXiv preprint arXiv:1403.6162
- Kaniadakis, G. 2009, *Eur. Phys. J. A*, 40, 275
- Kaufmann, R. L. & Paterson, W. R. 2006, *J. Geophys. Res.*, 111, A10214
- . 2009, *J. Geophys. Res.*, 114, A00D04
- . 2011, *J. Geophys. Res.*, 116, A08206
- Kivelson, M. G. & Russell, C. T., eds. 1995, *Introduction to Space Physics* (Cambridge University Press)
- Klein, K. G., Howes, G. G., & TenBarge, J. M. 2017, *Journal of Plasma Physics*, 83
- Klimchuk, J. A. 2006, *Solar Phys.*, 234, 41
- Krall, N. A. 1997, *Adv. Space Res.*, 20, 715
- Krommes, J. A. & Hu, G. 1994, *Physics of plasmas*, 1, 3211
- Leubner, M. P. 2004, *Phys. Plasmas*, 11, 1308
- Li, T. C., Howes, G. G., Klein, K. G., & TenBarge, J. M. 2016, *Ap. J. Lett.*, 832, L16
- Liang, H. et al. in prep., TBD
- Liu, Y.-H., Birn, J., Daughton, W., Hesse, M., & Schindler, K. 2014, *J. Geophys. Res.*, 119, 9773
- Loureiro, N. F., Schekochihin, A. A., & Zocco, A. 2013, *Phys. Rev. Lett.*, 111, 025002
- Lyubarsky, Y. & Kirk, J. G. 2001, *Ap. J.*, 547, 437
- Ma, X. & Otto, A. 2014, *J. Geophys. Res.*, 119, 5575
- Margolin, L. G. 2017, *Entropy*, 19, 368
- Mouhot, C. & Villani, C. 2011, *Acta mathematica*, 207, 29
- Nakata, M., Watanabe, T.-H., & Sugama, H. 2012, *Phys. Plasmas*, 19, 022303
- Naval Research Laboratory Plasma Physics Division, ed. 2018, *NRL Plasma Formulary No. NRL/PU/6790-18-640* (Naval Research Laboratory)
- Numata, R. & Loureiro, N. F. 2015, *J. Plasma Physics*, 81, 305810201
- Olivier, C. P., Engelbrecht, N. E., & Strauss, R. D. 2018, *J. Geophys. Res.*, doi:10.1029/2018/JA026102
- Parashar, T. N., Shay, M. A., Cassak, P. A., & Matthaeus, W. H. 2009, *Phys. Plasmas*, 16, 032310
- Parks, G. K., Lee, E., McCarthy, M., Goldstein, M., Fu, S. Y., Cao, J. B., Canu, P., Lin, N., Wilber, M., Dandouras, I., Réme, H., & Fazakerley, A. 2012, *Phys. Rev. Lett.*, 106, 061102
- Planck, M. *Entropie und Wahrscheinlichkeit*, In *Vorlesungen über die theorie der wurmestrahlung* (J. A Barth: Leipzig, Germany)
- Priest, E. R. & Forbes, T. R. 2002, *Astron. Astrophys. Rev.*, 10, 313
- Reynolds, S. P. 2008, *Ann. Rev. Astron. Astrophys.*, 46, 89
- Rosenberg, M. J., Li, C. K., Fox, W., Zylstra, A. B., Stoeckl, C., Séguin, F. H., Frenje, J. A., & Petrasso, R. D. 2015, *Phys. Rev. Lett.*, 114, 205004
- Rowan, M. E., Sironi, L., & Narayan, R. 2017, *Ap. J.*, 850, 29
- Sanchez, E. R., Wing, S., Spanswick, E., & Donovan, E. 2012, *J. Geophys. Res.*, 117, A05226
- Sarazin, Y., Dif-Pradalier, G., Zarzoso, D., Garbet, X., Ghendrih, P., & Grandgirard, V. 2009, *Plasma Phys. Control. Fusion*, 51, 115003
- Schekochihin, A., Cowley, S., Dorland, W., Hammett, G., Howes, G., Quataert, E., & Tatsuno, T. 2009, *The Astrophysical Journal Supplement Series*, 182, 310
- Servidio, S., Chasapis, A., Matthaeus, W., Perrone, D., Valentini, F., Parashar, T., Veltri, P., Gershman, D., Russell, C., Giles, B., et al. 2017, *Physical review letters*, 119, 205101
- Shannon, C. E. 1948, *The Bell System Technical Journal*, 27, 379
- Shay, M. A., Drake, J. F., & Swisdak, M. 2007, *Phys. Rev. Lett.*, 99, 155002
- Sironi, L., Giannios, D., & Petropoulou, M. 2016, *Monthly Notices of the Royal Astronomical Society*, 462, 48
- Sironi, L. & Spitkovsky, A. 2014, *Ap. J. Lett.*, 783, L21

- Sitnov, M. I., Merkin, V. G., Roytershteyn, V., & Swisdak, M. 2018, *Geophys. Res. Lett.*, 45, 4639
- Swisdak, M. 2016, *Geophys. Res. Lett.*, 43, 43
- Tatsuno, T., Dorland, W., Schekochihin, A., Plunk, G., Barnes, M., Cowley, S., & Howes, G. 2009, *Physical review letters*, 103, 015003
- TenBarge, J. M. & Howes, G. G. 2012, *Phys. Plasmas*, 19, 055901
- . 2013, *Ap. J. Lett.*, 771, L27
- Told, D., Jenko, F., TenBarge, J., Howes, G., & Hammett, G. 2015, *Phys. Rev. Lett.*, 115, 025003
- Trottenberg, U., Oosterlee, C. W., & Schuller, A. 2000, *Multigrid* (Academic Press, San Diego)
- Tsallis, C. 1988, *J. Stat. Phys.*, 52, 479
- Tsurutani, B. T. & Stone, R. G., eds. 2013, *Collisionless Shocks in the Heliosphere: Reviews of Current Research, Volume 35*, Geophysical Monograph Series (American Geophysical Union)
- Vaivads, A., Retinó, A., Soucek, J., Khotyaintsev, Y. V., Valentini, F., Escoubet, C. P., Alexandrova, O., André, M., Bale, S. D., Balikhin, M., & et al. 2016, *Journal of Plasma Physics*, 82
- Wan, M., Matthaeus, W. H., Roytershteyn, V., Parashar, T. N., Wu, P., & Karimabadi, H. 2016, *Physics of Plasmas*, 23, 042307
- Wang, C.-P., Lyons, L. R., Wolf, R. A., Nagai, T., Weygand, J. M., & Lui, A. T. Y. 2009, *J. Geophys. Res.*, 114, A00D02
- Watanabe, T.-H. & Sugama, H. 2004, *Phys. Plasmas*, 11, 1476
- Wolf, R. A., Kumar, V., Toffoletto, F. R., Erickson, G. M., Savoie, A. M., Chen, C. X., & Lemon, C. L. 2006, *J. Geophys. Res.*, 111, A12218
- Wolf, R. A., Wan, Y., Xing, X., Zhang, J.-C., & Sazykin, S. 2009, *J. Geophys. Res.*, 114, A00D05
- Yang, Y., Matthaeus, W. H., Parashar, T. N., Haggerty, C. C., Roytershteyn, V., Daughton, W., Wan, M., Shi, Y., & Chen, S. 2017a, *Physics of Plasmas*, 24, 072306
- Yang, Y., Matthaeus, W. H., Parashar, T. N., Wu, P., Wan, M., Shi, Y., Chen, S., Roytershteyn, V., & Daughton, W. 2017b, *Phys. Rev. E*, 95, 061201
- Zeiler, A., Biskamp, D., Drake, J. F., Rogers, B. N., Shay, M. A., & Scholer, M. 2002, *J. Geophys. Res.*, 107, 1230
- Zenitani, S., Hesse, M., Klimas, A., & Kuznetsova, M. 2011, *Phys. Rev. Lett.*, 106, 195003